A high-order target phase approach for the station-keeping of periodic orbits

Xiaoyu Fu[1] (✉), **Nicola Baresi**[1], **and Roberto Armellin**[2]

1. Surrey Space Centre, University of Surrey, Guildford, GU2 7XH, UK
2. Te Pūnaha Ātea - Auckland Space Institute, University of Auckland, Auckland 1010, New Zealand

ABSTRACT

A novel high-order target phase approach (TPhA) for the station-keeping of periodic orbits is proposed in this work. The key elements of the TPhA method, the phase-angle Poincaré map and high-order maneuver map, are constructed using differential algebra (DA) techniques to determine station-keeping epochs and calculate correction maneuvers. A stochastic optimization framework tailored for the TPhA-based station-keeping process is leveraged to search for fuel-optimal and error-robust TPhA parameters. Quasi-satellite orbits (QSOs) around Phobos are investigated to demonstrate the efficacy of TPhA in mutli-fidelity dynamical models. Monte Carlo simulations demonstrated that the baseline QSO of JAXA's Martian Moons eXploration (MMX) mission could be maintained with a monthly maneuver budget of approximately 1 m/s.

1 Introduction

Over the past decades, periodic orbits derived from the restricted three-body problem (RTBP) have been extensively employed as nominal trajectories in different deep space missions. To counteract the adverse effects of diverse perturbations in real mission environments, various station-keeping strategies have been designed specifically for periodic orbits to achieve long-term orbital maintenance [1–4]. Regarding the geometric symmetry of a periodic orbit, the x-axis crossing control strategy was developed to target certain conditions when intersecting the orbit's symmetry/near-symmetry plane [5]. Using the monodromy matrix of a periodic orbit, the stable and unstable modes for nominal motion are identified, and a Floquet mode controller can be designed to counteract the unstable mode [6]. A similar idea was adopted in the development of the Hamiltonian structure-preserving strategy, in which the expression of a corrective maneuver was achieved by leveraging the stable and unstable instantaneous modes of a periodic orbit [7].

Among the existing station-keeping strategies, the target point approach (TPA) was initially introduced to compute correction maneuvers by minimizing a weighted cost function that includes maneuvers and position/velocity deviations from a nominal trajectory [8]. Multiple targeting strategies were derived from the TPA method and have been widely adopted in different mission scenarios [9–11]. However, it has also been validated that the classic TPA underperforms in the station-keeping of periodic orbits dominated by fast dynamics, for example, the quasi-satellite orbits (QSOs) adopted in the Martian Moons eXploration (MMX) mission [12]. In this case, three limitations of the TPA method are recognized: a low tolerance to navigation error level (3σ errors derived from MMX covariance analyses can be unacceptable) [13], a substantial percentage of failed Monte Carlo (MC) runs (over 50% exceed the maximum threshold for the position residual) [12], and a significantly higher maneuver budget in comparison to other station-keeping methods, for example, the station-keeping method developed using convex optimization [14].

A close inspection of the TPA-based station-keeping process for a QSO around Phobos can elucidate the underlying causes of the TPA's ineffectiveness; a corresponding illustration is provided in Fig. 1. The left subplot in Fig. 1 shows a typical TPA-based station-
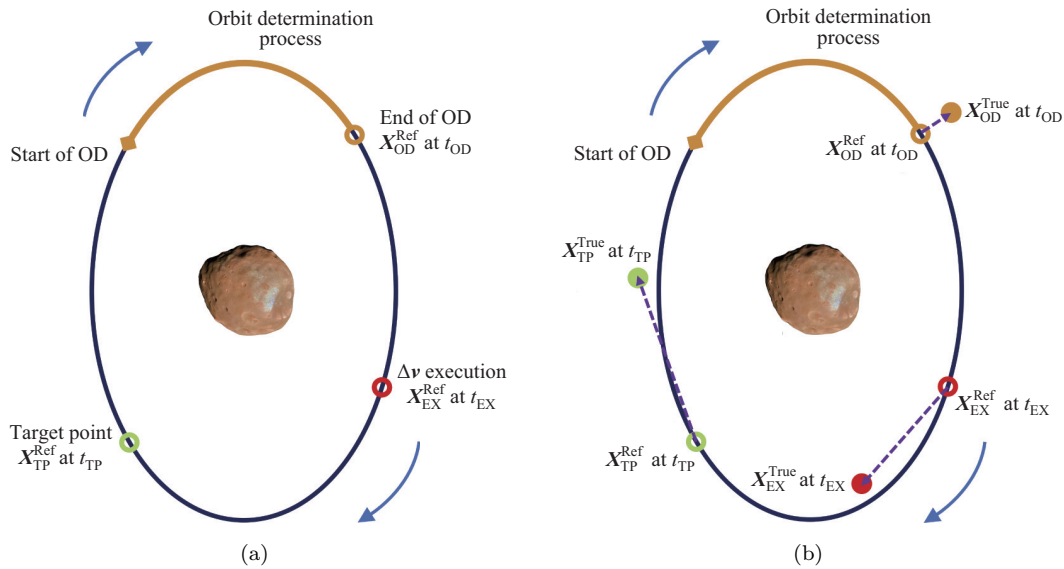
Fig. 1 Illustration of TPA-based station-keeping process for a QSO. (a) A typical TPA-based station-keeping process with reference states marked by empty circles on a QSO. (b) A failed TPA-based station-keeping process resulting from a perturbation at the OD epoch.

keeping process, where an orbit determination (OD) is performed initially, and a subsequent correction maneuver is executed at a predetermined epoch in order to minimize the state residual at a target point. When insertion and navigation errors are considered, it is noticeable that owing to the fast dynamics, the perturbed true state at an initial OD epoch can result in large downstream state deviations. As shown in the right-side subplot of Fig. 1, the true states at maneuver execution (EX) epoch and target point epoch are remote from their corresponding reference states, although they are still located in the vicinity of the reference trajectory. In such a scenario, a large-angle maneuver must still be performed to reduce the state deviation at a target epoch. This maneuver is superfluous and even counterproductive, as the true states remain close to a nominal orbit.

To overcome the aforementioned deficiencies of the classic TPA, a novel high-order target phase approach (TPhA) is proposed. Instead of defining station-keeping epochs timewise, in the TPhA method, critical station-keeping epochs are determined by reaching a certain surface of the section along a candidate periodic orbit. Accordingly, a phase-angle Poincaré map is derived to satisfy the strict requirement of reaching any prescribed surface of a section during orbital propagation. A high-order maneuver map is further established based on the phase-angle Poincaré map to enable the accurate

calculation of correction maneuvers. These two maps form the backbone of the proposed high-order TPhA method. The fuel optimality and error robustness of the TPhA method are further investigated using a stochastic optimization framework tailored for the TPhA-based station-keeping process.

Based on these research objectives, this paper is structured as follows. We begin with an introduction to the dynamical and gravitational models adopted in this study. Subsequently, the novel TPhA method is proposed. The construction of the two aforementioned maps is elaborated upon and a stochastic optimization scheme to determine the related TPhA parameters is provided. We then describe a follow-up station-keeping analysis for candidate QSOs performed to evaluate TPhA's effectiveness of in autonomous dynamics. The proposed methodology is further extended to higher-fidelity models to investigate its feasibility in realistic mission scenarios. Finally, conclusions are presented in Section 6 of this paper.

2 Dynamical and gravitational models

In this section, the circular restricted three-body problem (CRTBP) and the elliptic restricted three-body problem (ERTBP) are summarized. Subsequently, the gravitation modelling of an ellipsoidal celestial body is presented for

a more accurate station-keeping analysis.

2.1 Circular restricted three-body problem

In the CRTBP, it is hypothesized that the motion of a particle m with a negligible mass is dominated by the gravitation of two primary bodies, m_1 and m_2, which are in a circular orbit around each other. Typically, the motion of the particle is investigated in a rotating coordinate frame, where the barycenter of the two bodies (i.e., the primaries) is taken as the origin of the system, and the x-axis is chosen such that the two primaries remain stationary along this axis. In addition, a set of normalized units is customarily applied: The length unit is selected to match the constant distance between the two masses, the unit of mass is chosen to be the sum of m_1 and m_2, and the time unit is chosen such that the orbital period of the two primary bodies about their barycenter is equal to 2π. After this normalization, the only remaining parameter of the system is the mass ratio parameter, μ, which is given by

$$\mu = \frac{m_2}{m_1 + m_2}$$

The equations of motion (EOMs) for the CRTBP in the rotating coordinate frame are [15]:

$$\begin{cases} \ddot{x} - 2\dot{y} = -\bar{U}_x \\ \ddot{y} + 2\dot{x} = -\bar{U}_y \\ \ddot{z} = -\bar{U}_z \end{cases} \quad (1)$$

where (x, y, z) and $(\dot{x}, \dot{y}, \dot{z})$ denote the position and velocity components, respectively, of a particle in the rotating frame. $\bar{U}$ corresponds to the effective potential and is defined as

$$\bar{U} = -\frac{1}{2}(x^2 + y^2) + U_1(x,y,z) + U_2(x,y,z) - \frac{1}{2}\mu_1\mu_2 \quad (2)$$

where $\mu_1 = (1 - \mu)$ and $\mu_2 = \mu$ represent the normalized masses of the two primaries. $U_i(x,y,z) = -\mu_i/r_i$ ($i = 1, 2$) denotes the gravitational potential of the i-th

primary body, and r_i is the distance from the particle to the corresponding primary. The subscript of $\bar{U}$ in EOMs denotes the corresponding partial derivatives. It can be proven that the CRTBP is an autonomous (time-invariant) system with one integral of motion, known as the Jacobi constant:

$$C(x,y,z,\dot{x},\dot{y},\dot{z}) = -(\dot{x}^2 + \dot{y}^2 + \dot{z}^2) - 2\bar{U}(x,y,z) \quad (3)$$

2.2 Elliptic restricted three-body problem

A natural generalization of the CRTBP is the ERTBP, in which the motion of a mass particle is governed by two primaries m_1 and m_2, which orbit elliptically about their barycenter with eccentricity e [16] (see Fig. 2). To investigate the mass particle's motion in a rotating frame, the true anomaly $f(t)$ of m_2's orbit is introduced. Normalizing the system of units such that the distance between the two primaries at $f = \pi/2$ is unity and the primaries have unit angular momentum, a typical barycentric pulsating rotating coordinate frame O–xyz is established, in which m_1 and m_2 are fixed at $(-\mu, 0, 0)$ and $(1 - \mu, 0, 0)$, respectively. By designating the true anomaly f as the independent variable of the system, the EOMs of the ERTBP in this pulsating rotating coordinate frame take the form [16]:

$$\begin{cases} x'' - 2y' = -\bar{\omega}_x \\ y'' + 2x' = -\bar{\omega}_y \\ z'' + z = -\bar{\omega}_z \end{cases} \quad (4)$$

where the superscript $'$ denotes differentiation with respect to f; $\bar{\omega} = \bar{\Omega}/(1 + e\cos f)$ corresponds to the effective potential of the ERTBP, its subscripts denote its corresponding partial derivatives, and

$$\bar{\Omega} = -\frac{1}{2}(x^2 + y^2 + z^2) + U_1(x,y,z) +$$
$$U_2(x,y,z) - \frac{1}{2}\mu_1\mu_2 \quad (5)$$

where $U_i(x,y,z) = -\mu_i/r_i$ ($i = 1, 2$) denotes the gravitational potential of the i-th primary body in the
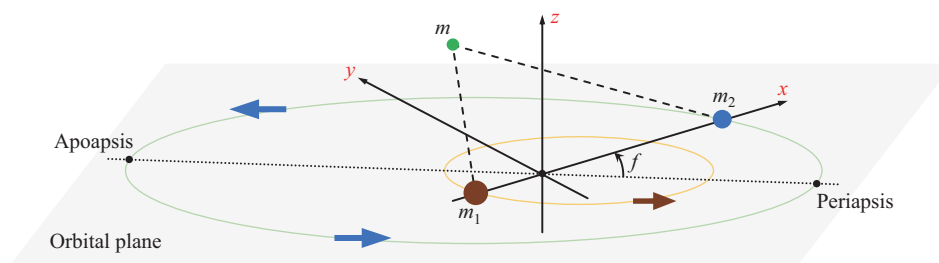

Fig. 2 Illustration of the ERTBP.

pulsating rotating frame. Owing to the existence of the time-varying effective potential $\bar{\omega}$, the ERTBP is a non-autonomous system; thus, it does not possess the Jacobi constant. Note that when $e = 0$, the choice of units gives $f = t$, so that Eq. (4) is reduced to Eq. (1) of the CRTBP.

2.3 Ellipsoidal gravitation model

As illustrated in Sections 2.1 and 2.2, for both the CRTBP and ERTBP, the nonlinear terms on the right-hand side of their EOMs are derived from the normalized gravitational potential of a point-mass secondary. This approximation is sufficient for the preliminary design of transfers between different planets in the solar system [15]. However, considering close-proximity operations around a celestial body, especially scientific missions around a small body with an irregular shape (e.g., JAXA's MMX mission), the gravitation calculated from the aforementioned point-mass secondary is not sufficient for in-depth astrodynamical analysis, and thus more accurate gravitation modelling is necessary.

Among existing gravitation models for non-spherical celestial bodies, the ellipsoidal gravitation model has been validated and is widely applied in multiple mission scenarios [17]. It utilizes ellipsoidal harmonic expansions to represent a potential field that can accurately model the potential adjacency to a celestial body's surface. Here, a concise summary of the gravitation modelling of a constant-density ellipsoidal body is provided, with its gravitational potential given by

$$U_2(X, Y, Z) = -\mu_2 \frac{3}{4} \int_0^\infty \phi(X, Y, Z, l + \Lambda) \frac{\mathrm{d}l}{\Delta(l + \Lambda)} \tag{6}$$

where X, Y, and Z correspond to the coordinates of a mass particle as observed from the principal-axis frame of the body. Furthermore,

$$\Delta(l + \Lambda) = \sqrt{(\bar{\alpha}^2 + \Lambda + l)(\bar{\beta}^2 + \Lambda + l)(\bar{\gamma}^2 + \Lambda + l)} \tag{7a}$$

$$\phi(X, Y, Z, l + \Lambda) = \frac{X^2}{\bar{\alpha}^2 + \Lambda + l} + \frac{Y^2}{\bar{\beta}^2 + \Lambda + l} + \frac{Z^2}{\bar{\gamma}^2 + \Lambda + l} - 1 \tag{7b}$$

where $\bar{\alpha}$, $\bar{\beta}$, and $\bar{\gamma}$ are the largest, intermediate, and smallest semi-major axes of the body, respectively, and Λ is defined as the nonnegative root of $\phi(X, Y, Z, \Lambda) = 0$. Note that the elliptic integrals in Eq. (6) can be efficiently

calculated using the numerical procedures provided in Ref. [18].

3 High-order target phase approach

In this section, the concept of the TPhA is introduced. Compared with the classic TPA, the TPhA achieves improvements in the determination of station-keeping epochs and the calculation of correction maneuvers. Both advancements are realized by the application of two high-order maps, the phase-angle Poincaré map and high-order maneuver map, which are generated using DA techniques. A stochastic optimization scheme is employed to determine the related station-keeping parameters when considering different sources of uncertainties.

3.1 Definition of target phase approach

The states along a periodic orbit can be individually parameterized using different phase angles. The TPhA method uses such a geometric property to compute the impulsive station-keeping maneuvers of a spacecraft with respect to a nominal periodic orbit by solving a linear-quadratic regulator problem. Let the i-th surface of the section to execute the i-th correction maneuver be located at a phase angle θ_{EX_i}; then, the optimal maneuver $\Delta \boldsymbol{v}_i$ is solved by minimizing the cost function in Eq. (8):

$$J = \sum_{i=1}^m \Delta \boldsymbol{v}_i^{\mathrm{T}} \Delta \boldsymbol{v}_i + \sum_{j=1}^n \boldsymbol{p}_j^{\mathrm{T}} R_j \boldsymbol{p}_j + \sum_{j=1}^n \boldsymbol{q}_j^{\mathrm{T}} S_j \boldsymbol{q}_j \tag{8}$$

where the superscript T denotes the transpose; $\Delta \boldsymbol{v}_i$ denotes the maneuver at θ_{EX_i}; $\boldsymbol{p}_j$ and $\boldsymbol{q}_j$ denote the predicted position and velocity residuals at a specified downstream surface of section θ_{TP_j}, respectively; and the symmetric positive semi-definite R_j and S_j are the weighting matrices of the position and velocity deviations at section θ_{TP_j}, respectively. In the TPhA, the sections $\{\theta_{\mathrm{TP}_j}\}_{j=1}^n$ are called the target phases (TPh).

In comparison with the classic TPA method, in which station-keeping epochs are fixed during a given duration, the station-keeping epochs in the TPhA are defined by Poincaré sections, that is, each station-keeping epoch is determined by the moment when a prescribed phase angle is reached. A simple example of the TPhA-based station-keeping process is illustrated in Fig. 3, where three separate Poincaré sections are defined by different phase angles to determine the corresponding station-keeping epochs. The OD process is terminated at section θ_{OD}. During the station-keeping process, a maneuver
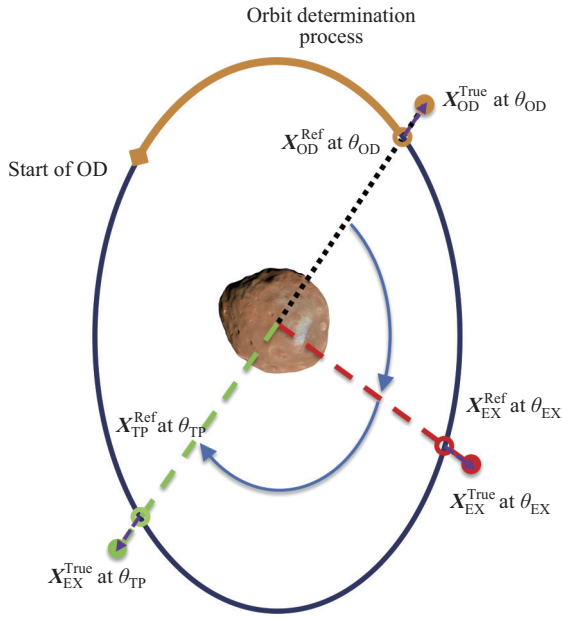
Fig. 3 Illustration of a station-keeping process based on the TPhA.

is not executed until section θ_{EX} is reached, and the location of the target state is now entirely dependent on section θ_{TP}. In contrast to the classic TPA method, in which all downstream states are determined at fixed TPA epochs regardless of the state deviation at an OD epoch, in the TPhA method, the crucial station-keeping epochs become flexible timewise, and perturbations in the OD state bring about variations in the downstream station-keeping epochs. However, the strict requirement of reaching the target Poincaré sections must be satisfied.

3.2 Phase-angle Poincaré map

The TPhA method necessitates the application of the phase-angle Poincaré map and the introduction of a relevant concept, the Poincaré section. A Poincaré section is the intersection of a periodic orbit in the phase space of a dynamical system with a lower-dimensional subspace that is transverse to the flow of the system. The corresponding Poincaré map of the Poincaré section can be represented by a high-order polynomial map built using DA techniques [19]. It can map any point in the neighborhood of a reference point $\boldsymbol{X}_0^*$ onto a target Poincaré section defined by phase angle θ^*. To build this map, the reference time span t^* for a reference state $\boldsymbol{X}_0^*$ to reach the target Poincaré section is first determined. Subsequently, the independent time variable t in the standard EOMs is substituted with $\tau = t/t^*$ and the augmented EOMs in Eq. (9) are employed:

$$
\begin{cases}
\dfrac{\mathrm{d}\boldsymbol{X}}{\mathrm{d}\tau} = t^* f(\boldsymbol{X}) \\[2mm]
\dfrac{\mathrm{d}l}{\mathrm{d}\tau} = 0
\end{cases}
\tag{9}
$$

where the adjoint variable l satisfies the condition $l(0) = t^*$. Using the augmented EOMs, a reference state $\boldsymbol{X}_0^*$ is transformed into $\boldsymbol{X}_{0,\text{aug}}^* = [\boldsymbol{X}_0^*, t^*]$. For differentiation, a state in the neighborhood of $\boldsymbol{X}_{0,\text{aug}}^*$ is denoted by $\boldsymbol{X}_{0,\text{aug}} = [\boldsymbol{X}_0, t_{\text{f}}]$. By initializing the full state vector of $\boldsymbol{X}_{0,\text{aug}}$ as DA variables and propagating the dynamics in Eq. (9) from $\tau = 0$ to $\tau = 1$, the Taylor polynomial map in Eq. (10) is established:

$$
\boldsymbol{X}_{\text{f,aug}} = \mathcal{T}_{\boldsymbol{X}_{\text{f,aug}}}(\boldsymbol{X}_0, t_{\text{f}})
\tag{10}
$$

where the augmented final state $\boldsymbol{X}_{\text{f,aug}}$ corresponds to a point in the vicinity of a target Poincaré section θ^*. With the first two elements in $\boldsymbol{X}_{\text{f,aug}}$, x_{f} and y_{f}, the phase angle of the final state θ_{f} can be expressed as

$$
\theta_{\text{f}} = \arctan\left(\frac{y_{\text{f}}}{x_{\text{f}}}\right) = \mathcal{T}_{\theta_{\text{f}}}(\boldsymbol{X}_0, t_{\text{f}})
\tag{11}
$$

Applying the phase angle constraint $\theta_{\text{f}} - \theta^* = 0$ to remove the t_{f} degree of freedom and partially inverting the map in Eq. (11) [12] yields

$$
t_{\theta^*} = \mathcal{T}_{t_{\theta^*}}(\boldsymbol{X}_0)
\tag{12}
$$

which delivers the propagation time t_{θ^*} to reach a target Poincaré section θ^* based on the initial state $\boldsymbol{X}_0$. Furthermore, Eq. (12) can be substituted back into the map in Eq. (10) to obtain

$$
\boldsymbol{X}_{\theta^*} = \mathcal{T}_{\boldsymbol{X}_{\theta^*}}(\boldsymbol{X}_0)
\tag{13}
$$

Equations (12) and (13) jointly compose the phase-angle Poincaré map, in which both the propagated states on a target Poincaré section and the corresponding propagation time can be accurately calculated using polynomial evaluations. Note that the map inversion technique employed in Eq. (11) is already embedded in the existing DA toolbox. It has been proven that as long as the inverse of the linear part of a polynomial map exists, the inversion of the polynomial map can be performed. We refer readers interested in the underlying algorithm to the work of Berz [20].

3.3 High-order maneuver map

Once accurately propagated states on the prescribed Poincaré sections are achieved, a high-order maneuver map can be built to efficiently calculate accurate TPhA maneuvers. The maneuver map is constructed using the aforementioned partial inversion technique, and

the corresponding procedures are as follows: Following the orbital maintenance process illustrated in Fig. 3, the gradient of the cost function J in Eq. (8) can be represented as a function of the optimal TPhA maneuver $\Delta \boldsymbol{v}$ and the state $\boldsymbol{X}_0$ at the OD surface of section θ_{OD}: $\nabla J = \nabla J(\Delta \boldsymbol{v}, \boldsymbol{X}_0)$. A manifest solution of $\nabla J = \boldsymbol{0}$ is $(\boldsymbol{0}_{3\times1}, \boldsymbol{X}_0^{\mathrm{Ref}})$, where $\boldsymbol{X}_0^{\mathrm{Ref}}$ denotes the reference state at θ_{OD}. Based on this trivial solution, the other solutions $(\Delta \boldsymbol{v}^*, \boldsymbol{X}_0^*)$ can be computed using the nonlinear impulsive maneuver solver proposed by Fu et al. [21]. Subsequently, the increment of ∇J at a given zero $(\Delta \boldsymbol{v}^*, \boldsymbol{X}_0^*)$ can be acquired by expanding ∇J as a high-order Taylor polynomial map, resulting in

$$\delta \nabla J = \mathcal{T}_{\delta \nabla J}(\delta \Delta \boldsymbol{v}, \delta \boldsymbol{X}_0) \tag{14}$$

where δ represents the increment of a variable. Applying partial inversion to the map in Eq. (14) yields

$$\delta \Delta \boldsymbol{v} = \mathcal{T}_{\delta \Delta \boldsymbol{v}}(\delta \nabla J\,|_{\Delta \boldsymbol{v}}, \delta \boldsymbol{X}_0) \tag{15}$$

where $\delta \nabla J\,|_{\Delta \boldsymbol{v}}$ denotes the gradient components with respect to $\Delta \boldsymbol{v}$. By enforcing $\delta \nabla J\,|_{\Delta \boldsymbol{v}} = \boldsymbol{0}$ for $\forall \delta \boldsymbol{X}_0$ in Eq. (15), the map in Eq. (16) is obtained:

$$\delta \Delta \boldsymbol{v} = \mathcal{T}_{\delta \Delta \boldsymbol{v}}(\delta \boldsymbol{X}_0) \tag{16}$$

which can be substituted into $\Delta \boldsymbol{v} = \mathcal{T}_{\Delta \boldsymbol{v}}(\delta \Delta \boldsymbol{v})$ and finally provides

$$\Delta \boldsymbol{v} = \mathcal{T}_{\Delta \boldsymbol{v}}(\delta \boldsymbol{X}_0) \tag{17}$$

Equation (17) establishes a relationship between the optimal high-order maneuver $\Delta \boldsymbol{v}$ and the arbitrary $\delta \boldsymbol{X}_0$ errors within the convergence domain of Eq. (17). Note that the construction of a maneuver map in Eq. (17) is based on an established phase-angle Poincaré map and no repeated orbit propagation is required.

3.4 Determination of TPhA parameters

To adopt the TPhA method for station-keeping analysis, relevant TPhA parameters must be determined, including the different phases along a candidate periodic orbit and the weighting matrices in the cost function J in Eq. (8). In addition, considering the existence of uncertainties during orbital maintenance, the error robustness of the TPhA parameters must be considered [22]. Hence, a stochastic optimization scheme [12] is employed to search for error-robust optimal TPhA parameters for the station-keeping of periodic orbits.

In a stochastic optimization scheme designed for station-keeping, three major sources of uncertainty

are considered: orbit injection (OI) errors $\{\boldsymbol{\epsilon}_{\mathrm{OI}}\}$, OD errors $\{\boldsymbol{\epsilon}_{\mathrm{OD}}\}$, and EX errors $\{\boldsymbol{\epsilon}_{\mathrm{EX}}\}$. For a stochastic optimization scheme adapted for the TPhA method, the station-keeping process is divided into multiple sequential TPhA loops by taking advantage of the periodicity of a periodic orbit. A TPhA loop is defined as the interval between two consecutive OD sections, and its length can be defined as the number of orbital periods between the two OD sections. This justifies the relatively fixed TPhA phases for each TPhA loop, and further allows the phase-angle Poincaré maps and a high-order maneuver map generated for one TPhA loop to be recycled for all remaining loops. Apart from the utilization of periodicity, another prerequisite that dominates the performance of the proposed stochastic optimization scheme is the location of the OD sections. In our previous work, we quantitatively demonstrated that to minimize the growth of OD errors, the section where an apoapsis is located should be selected as the OD position for the orbital maintenance of a periodic orbit in the CRTBP [12]. Here, the same strategy was adopted for station-keeping analysis based on the TPhA method.

Based on the two aforementioned prerequisites, the TPhA parameters can be searched for through global optimization using embedded MC simulations. The design variables of this optimization include the phase angles θ_{OD}, θ_{EX}, and θ_{TPh}, and the weights of the weighting matrices in the cost function J. Once a set of design variables is specified, the phase-angle Poincaré maps and maneuver map in Eq. (18) can be established:

$$\begin{cases} \boldsymbol{X}_{\theta_{\mathrm{EX}}} = \mathcal{T}_{\boldsymbol{X}_{\theta_{\mathrm{EX}}}}(\delta \boldsymbol{X}_{\theta_{\mathrm{OD}}}) \\ \boldsymbol{X}_{\theta_{\mathrm{OD}}} = \mathcal{T}_{\boldsymbol{X}_{\theta_{\mathrm{OD}}}}(\delta \boldsymbol{X}_{\theta_{\mathrm{EX}}}) \\ \Delta \boldsymbol{v} = \mathcal{T}_{\Delta \boldsymbol{v}}(\delta \boldsymbol{X}_{\theta_{\mathrm{OD}}}) \end{cases} \tag{18}$$

Note that, once generated for a single TPhA loop, the maps in Eq. (18) can be recycled by the remaining TPhA loops owing to the autonomy of the CRTBP and the periodicity of the orbit of interest. Hence, the time-consuming orbit propagation can be replaced by fast polynomial evaluations, and corrective maneuvers can be calculated efficiently. Furthermore, sufficiently large input state residual sets $\{\delta \boldsymbol{X}_{\theta_{\mathrm{OD}}}\}$ and $\{\delta \boldsymbol{X}_{\theta_{\mathrm{EX}}}\}$ can be easily handled, ensuring the error robustness of the acquired optimal TPhA parameters.

Finally, the fitness function of this stochastic optimization is defined as

$$J_{\mathrm{S/K}} = \|\Delta \boldsymbol{v}\|_{\mathrm{total}}^{99} + p_{\mathrm{f}} N_{\mathrm{fail}} \tag{19}$$

where the subscrip S/K stands for station-keeping, $\|\Delta v\|_{\text{total}}^{99}$ denotes the approximated 99th percentile of the total maneuver cost for all eligible MC runs, and p_{f} denotes a penalty factor that penalizes the influence of the number of failed MC runs N_{fail}. To illustrate the aforementioned procedures, the pseudocode for the fitness function of the TPhA is provided in Algorithm 1, where only one manuever phase θ_{EX} and one target phase θ_{TPh} are included. Such a stochastic optimization scheme is always feasible for the station-keeping analysis of periodic orbits in an autonomous system, where the maps in Eq. (18) generated by using DA techniques are sufficiently accurate [23, 24].

4 Station-keeping analyses in the CRTBP

In this section, candidate QSOs for station-keeping analysis are presented. The station-keeping configurations and global optimization setup are detailed, and the station-keeping results in the CRTBP and the corresponding findings are discussed.

4.1 Test cases: QSOs around Phobos

To evaluate the efficacy of the proposed TPhA method, QSOs around Phobos in the Mars–Phobos three-body system were selected as test cases. Ever since their discovery in 1969 [25], QSOs have been a major research focus owing to their linear stability and close proximity to the secondary body in a restricted three-body system. QSOs have been listed as candidate science orbits for multiple deep-space missions with close operations to celestial bodies, including ESA's DePhine [26] and NASA's JIMO [27]. Furthermore, five QSOs at low altitudes around Phobos are under extensive investigation by JAXA and are qualified for the proximity phase in the upcoming MMX mission, whereby the dynamical and geophysical environment of Phobos will be explored in great detail [28].

The QSO family around Phobos generated in the CRTBP is presented in Fig. 4. As shown in the figure, the QSOs can reach extremely low altitudes with respect to the surface of the Martian moon. Likewise, a similar QSO family can also be generated when the mass distribution of Phobos is modeled as an ellipsoid, which is more accurate in terms of the true shape of the Martian moon. The relevant physical parameters of Phobos are provided

---

Algorithm 1 Fitness function of the stochastic optimization for TPhA parameters

function FITNESS_SK_TPHA $(\theta_{\text{EX}}, \theta_{\text{TPh}}, R, S, \boldsymbol{X}_{\text{OI}}^{\text{Ref}},$
 $N_{\text{loop}}, \{\boldsymbol{\epsilon}_{\text{OI}}\}, \{\boldsymbol{\epsilon}_{\text{OD}}\}, \{\boldsymbol{\epsilon}_{\text{EX}}\})$
  Build Poincaré maps: $\boldsymbol{X}_{\theta_{\text{EX}}} = \mathcal{T}_{\boldsymbol{X}_{\theta_{\text{EX}}}}(\delta \boldsymbol{X}_{\theta_{\text{OD}}}),$
   $\boldsymbol{X}_{\theta_{\text{OD}}} = \mathcal{T}_{\boldsymbol{X}_{\theta_{\text{OD}}}}(\delta \boldsymbol{X}_{\theta_{\text{EX}}})$
  Build maneuver map: $\Delta \boldsymbol{v} = \mathcal{T}_{\Delta \boldsymbol{v}}(\delta \boldsymbol{X}_{\theta_{\text{OD}}})$
  OI: $\{\boldsymbol{X}_{\text{OI}}^{\text{True}}\} \Leftarrow \boldsymbol{X}_{\text{OI}}^{\text{Ref}} + \{\boldsymbol{\epsilon}_{\text{OI}}\}, \{\boldsymbol{X}_{\theta_{\text{OD}}^{(1)}}^{\text{True}}\} \Leftarrow \{\boldsymbol{X}_{\text{OI}}^{\text{True}}\}$

  while $i \leqslant N_{\text{loop}}$ & $\{\delta \boldsymbol{X}^{\text{True}}\} \leqslant \Delta d_{\text{max}}$ **do**
    Step #1: Add OD errors $\{\boldsymbol{\epsilon}_{\text{OD}}\}$
       $\{\boldsymbol{X}_{\theta_{\text{OD}}^{(i)}}^{\text{Det}}\} \Leftarrow \{\boldsymbol{X}_{\theta_{\text{OD}}^{(i)}}^{\text{True}}\} + \{\boldsymbol{\epsilon}_{\text{OD}}\}$
    Step #2: Propagate true trajectory to θ_{EX}
       $\{\boldsymbol{X}_{\theta_{\text{EX}}^{(i)}}^{\text{True}}\} = \mathcal{T}_{\boldsymbol{X}_{\theta_{\text{EX}}}}(\{\delta \boldsymbol{X}_{\theta_{\text{OD}}^{(i)}}^{\text{True}}\})$
    Step #3: Compute maneuvers:
       $\{\Delta \boldsymbol{v}_{(i)}\} = \mathcal{T}_{\Delta \boldsymbol{v}}(\delta \boldsymbol{X}_{\theta_{\text{OD}}^{(i)}}^{\text{Det}})$
    Step #4: Add EX errors $\{\boldsymbol{\epsilon}_{\text{EX}}\}$
       $\{\Delta \boldsymbol{v}_{(i)}\} \Leftarrow \{\Delta \boldsymbol{v}_{(i)}\} + \{\boldsymbol{\epsilon}_{\text{EX}}\}$
    Step #5: Execute maneuvers $\{\Delta \boldsymbol{v}_{(i)}\}$
       $\{\boldsymbol{X}_{\theta_{\text{EX}}^{(i)}}^{\text{True}}\} \Leftarrow \{\boldsymbol{X}_{\theta_{\text{EX}}^{(i)}}^{\text{True}}\} + \{[\boldsymbol{0}_{3\times 1}; \Delta \boldsymbol{v}_{(i)}]\}$
    Step #6: Propagate true trajectory to θ_{OD}
       $\{\boldsymbol{X}_{\theta_{\text{OD}}^{(i+1)}}^{\text{True}}\} = \mathcal{T}_{\boldsymbol{X}_{\theta_{\text{OD}}}}(\{\delta \boldsymbol{X}_{\theta_{\text{EX}}^{(i)}}^{\text{True}}\})$
  end while
  Number of failed MC runs: N_{fail}
  Total maneuver cost of eligible MC runs:
   $\{\|\Delta \boldsymbol{v}\|_{\text{total}}\} \leftarrow \{\sum \|\Delta \boldsymbol{v}_{(i)}\|\}$
  Fitness value: $J_{\text{S/K}} = \|\Delta \boldsymbol{v}\|_{\text{total}}^{99} + p_{\text{f}} N_{\text{fail}}$
end function
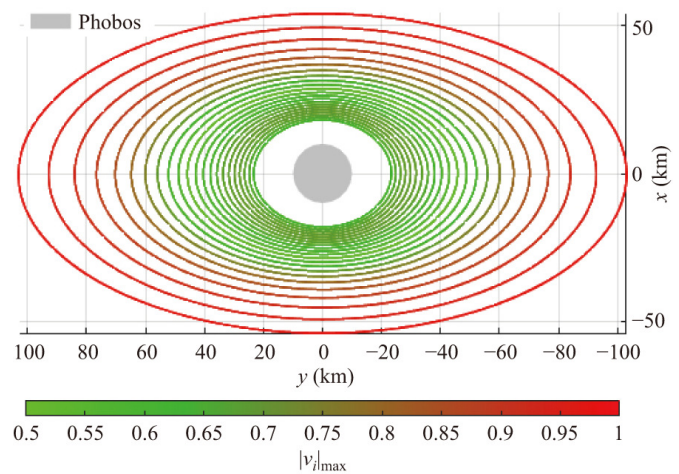
Fig. 4 QSOs around Phobos.

in Ref. [29]. In addition, procedures to transform the gravitational acceleration due to an ellipsoidal Phobos from its principal axis frame to a synodic rotating frame were elaborated by Baresi *et al.* [17].

The linear stability of QSOs is defined by the stability indices ν_i:

$$\nu_i = \frac{1}{2}\left(\lambda_i + \frac{1}{\lambda_i}\right), \; i = 1, 2 \qquad (20)$$

where λ_i and $\frac{1}{\lambda_i}$ comprise the reciprocal pair of eigenvalues of a monodromy matrix, that is, the state transition matrix (STM) integrated over one revolution. It has been validated that QSOs remain linearly stable across all altitude values because the maximum norm of their stability index is found to be no greater than one. In this study, three candidate QSOs for the MMX mission are selected, and their detailed orbital parameters are listed in Table 1. Notice that the subscripts apo and peri in Table 1 denote the apoapsis and periapsis of a QSO, respectively. The stability indices of each candidate QSO are provided alongside to showcase their linear stability.

4.2 Station-keeping configuration and optimization setup

The insertion and navigation errors provided by the covariance analysis for the MMX mission [13] are reported in Table 2, where a 3σ knowledge error of 150 m in position and 10 cm/s in velocity is considered. A percentage error model for maneuver execution is assumed, with a 3σ error of 3% applied in each velocity direction. According to the error modelling above, three error sets, the OI error set $\{\boldsymbol{\epsilon}_{\mathrm{OI}}\}$, OD error set $\{\boldsymbol{\epsilon}_{\mathrm{OD}}\}$, and EX error set $\{\boldsymbol{\epsilon}_{\mathrm{EX}}\}$, are generated before optimizing the TPhA parameters. Such predetermination of stochastic errors can avoid fluctuations in the fitness values resulting from varying optimization errors.

A genetic algorithm (GA) implemented in MATLAB was used to perform stochastic optimization of the TPhA parameters. GA optimization was performed in parallel, and the corresponding algorithm options are listed in Table 3. In addition, the number of MC samples used in each fitness evaluation was set to 1000. This MC sample size is sufficient to exhibit the statistical properties of the current uncertainty modelling and ensure the error robustness of the acquired TPhA parameters.

Table 3 Genetic algorithm options

Option	Value
Size of population	500
Maximum generations	250
Maximum simulation time	7 days
Crossover fraction	0.8
Creation function	Nonlinear feasible
Fitness scaling	Linear proportional
Parent selection	Tournament rule with 4 individuals
Mutation strategy	Adaptive feasible
Crossover strategy	Heuristic with coefficient $u = 1.2$

4.3 Simulation results and analyses

First, stochastic optimizations were executed for the three candidate QSOs in the CRTBP to search for the optimal TPhA parameters. In this case, the simplest TPhA scenario was applied, where in each TPhA loop, only one maneuver was applied to correct only the position residual at one target phase section. The surface section at the end of an OD process was selected at the apoapsis of a candidate QSO and θ_{OD} was defined as zero. Apart from the station-keeping configurations and optimization setup provided in the previous section, a maneuver frequency of approximately 48 h was employed, and the station-keeping duration was set to 30 days. Hence, the first month's station-keeping statistics could be obtained directly. Two levels of maximum allowable position residuals (10 and 5 km) were applied in separate station-keeping simulations. In addition, considering the practical limitations of the satellite propulsion system, two levels of minimum maneuver threshold, 1.50 and 0 mm/s, were assumed. If a computed maneuver had a magnitude less than the threshold, it was cancelled. The optimal TPhA parameters of the three candidate QSOs calculated using GA optimization are listed in Table 4, together with the number of failed MC runs

Table 1 Parameters of the candidate QSOs

	$r_{\mathrm{apo}} \times r_{\mathrm{peri}}$ (km)	$v_{\mathrm{apo}} \times v_{\mathrm{peri}}$ (m/s)	Orbital period (h)	Stability indices
QSO-La	48.84×30	8.68×15.31	5.76	$\nu_1 = -0.442, \nu_2 = 0.571$
QSO-Lb	30.81×22	8.25×12.79	4.40	$\nu_1 = -0.690, \nu_2 = 0.175$
QSO-Lc	26.69×20	8.31×12.31	3.97	$\nu_1 = -0.679, \nu_2 = 0.105$

Table 2 Insertion, navigation, and execution errors (3σ)

OI error in position	OI error in velocity	OD error in position	OD error in velocity	Execution error
150 m	10 cm/s	150 m	10 cm/s	3% in each direction

and the first month $\|\Delta\boldsymbol{v}\|_{\text{total}}^{99}$. In this table, the results from 12 independent optimizations are included, and all optimizations converge to a predetermined fitness function tolerance of 1×10^{-8}. It was confirmed that there was no failed MC run out of 1000 samples (i.e., $N_{\text{fail}} = 0$) for each station-keeping scenario.

According to Table 4, four main conclusions can be drawn. First, the monthly maneuver budget for the three candidate QSOs did not exceed 1 m/s. The candidates QSO-Lb and QSO-Lc allow control-free station-keeping strategies. Second, the maximum allowable position residual critically influences the maneuver budget. A larger allowable residual value corresponds to a smaller budget. Third, the maneuver thresholds used had no obvious influence on the maneuver budgets. Finally, there was no remarkable regularity in the selection of the TPhA phase sections.

To further investigate the performance of the TPhA, a more complex cost function was applied in which two maneuvers were executed in each TPhA loop to correct both the position and velocity residuals at a specified target phase section. Inspired by the results presented in Table 4, the most unruly QSO candidate, QSO-La, was selected, and the maximum position residual was fixed at 5 km. The maneuver threshold was removed, and the maneuver frequency varied discretely from one to eight orbital periods, which corresponds to a varied length of the TPhA loop from approximately 6 to 48 h. Instead of executing a 30-day station-keeping analysis, station-keeping was performed for 25 consecutive TPhA loops, from which a monthly maneuver budget was proportionally estimated. Moreover, the gravitation of Phobos was modeled with both a point mass and an ellipsoid to study the influence of the secondary's irregular gravity field. The corresponding results are labeled as "CRTBP" and "CRTBP+EPh" (where EPh represents ellipsoidal Phobos) in Table 5, where the results from eight independent stochastic optimizations are presented,

Table 4 Optimal TPhA parameters for candidate QSOs in the CRTBP

Candidate QSO	Maximum residual (km)	Maneuver threshold (mm/s)	1st month $\|\Delta\boldsymbol{v}\|_{\text{total}}^{99}$ (m/s)	Failed cases	θ_{EX} (orbital period)	θ_{TP} (orbital period)	R
QSO-La	10	1.50	0.128	0	0.756	1.412	0.021
		0	0.127	0	0.756	4.335	0.029
	5	1.50	0.207	0	0.985	7.294	0.124
		0	0.208	0	0.921	4.316	0.164
QSO-Lb	10	1.50	0	—	—	—	—
		0	0	—	—	—	—
	5	1.50	0	—	—	—	—
		0	0	—	—	—	—
QSO-Lc	10	1.50	0	—	—	—	—
		0	0	—	—	—	—
	5	1.50	0	—	—	—	—
		0	0	—	—	—	—

Table 5 Optimal TPhA parameters for QSO-La in autonomous systems

Orbital periods per loop	Length of one loop (h)	Dynamic model	Monthly maneuver budget (m/s)	Failed cases	θ_{EX1} (orbital period)	θ_{EX2} (orbital period)	θ_{TP} (orbital period)	R	S
1	5.77	CRTBP	0.305	0	0.747	0.748	1.335	1.02E−3	1.12E−7
		CRTBP+EPh	0.491	0	0.748	0.781	1.584	3.73E−3	3.46E−7
2	11.54	CRTBP	0.228	0	0.752	1.337	1.338	4.58E−3	3.72E−9
		CRTBP+EPh	0.286	0	0.757	1.443	1.444	1.19E−2	1.78E−7
4	23.08	CRTBP	0.143	0	0.744	0.746	2.843	3.86E−3	2.59E−4
		CRTBP+EPh	0.176	0	0.750	0.751	1.443	6.49E−3	1.82E−5
8	46.16	CRTBP	0.151	0	0.846	0.990	2.852	1.11E−5	1.17E−6
		CRTBP+EPh	0.362	0	0.877	1.528	2.908	2.36E−1	1.38E−1

all of which converge to a predetermined fitness function tolerance of 1×10^{-8}. Again, no failed MC runs occurred in the simulations for any of the achieved optimal TPhA parameters.

Information regarding multiple aspects is provided in Table 5. First, by increasing the length of each TPhA loop, the monthly maneuver budget experiences an initial decrease, followed by an increase when the maneuver frequency is decreased to approximately 48 h. Such a finding could guide the selection of maneuver frequency for real mission operations, as there is often a trade-off between maneuver cost and maneuver frequency. Second, in the comparison between the two different dynamics, the increment of the maneuver cost becomes more apparent when the TPhA loop is increased to eight orbital periods. This phenomenon is also understandable because the irregular gravitational field of Phobos causes more difficulty in station-keeping, and this challenge becomes tougher when corrective maneuvers are not applied in a timely manner. Third, an increasing regularity in the selection of phase sections emerges, as the 1st maneuvers are placed close to the periapsis of QSO-La, and the 2nd maneuvers are executed close to the periapsis or apoapsis of QSO-La. In comparison, the selections of the target phase sections do not exhibit an obvious tendency. Nevertheless, none of the target phase sections was placed in more than four orbital periods, which again indicates the necessity for timely maneuvers. In addition, the difference between the magnitudes of weights R and S indicates the dominance of position residuals in the TPhA method.

To further demonstrate the TPhA-based station-keeping process, the statistics of the position and velocity residuals of the two station-keeping scenarios in the last row of Table 5 are presented in Figs. 5 and 6, repsectively. The position and velocity residuals of all MC runs, $\{\delta_{\text{pos}}\}$ and $\{\delta_{\text{vel}}\}$, were recorded for 25 TPhA loops. The mean and standard deviation of δ_{pos} and δ_{vel}, denoted by μ and σ respectively, were also calculated, and are shown in the plots. The solid black line in each plot represents the variation in the mean of the position/velocity residual set with respect to the number of TPhA loops, and the shaded strips around the black line correspond to different multiples of the standard deviation. According to the two plots, the position and velocity deviations in both cases plateau after approximately five TPhA loops. The mean position and velocity deviations of the simulation based

on the CRTBP model becomes steady at 0.1 km and 0.04 m/s during the associate station-keeping process, respectively, and the position and velocity residuals of the other station-keeping simulation also reach relatively close levels. However, the standard deviations for both the position and velocity residuals of the latter case are larger than those of the former case, which should result from the gravitational perturbation of ellipsoidal Phobos. In addition, the different changing trends of the residuals in the two plots should be attributed to the collective influence of both the dynamics and the achieved optimal TPhA parameters.

5 Station-keeping analyses in the ERTBP

Following Section 4, the performance of the TPhA method was further evaluated using the ERTBP. The algorithm for applying a maneuver generated from the CRTBP to the ERTBP is introduced first. Then, the simulation results for the ERTBP are presented, and the corresponding findings are discussed.

5.1 Application of TPhA maneuvers in the ERTBP

After validating the efficacy of the TPhA in the autonomous CRTBP model, the performance of the maneuver maps generated by the TPhA was further evaluated in the high-fidelity ERTBP+EPh model to investigate their applicability in real-world spacecraft operations.

Notice that the maneuvering map in Eq. (18) was generated in the CRTBP with non-pulsating coordinates. Thus, to provide the input for the maneuver map, the states propagated using Eq. (4) must be transformed from pulsating to non-pulsating coordinates. Before executing this transformation, another conversion must be performed considering the usage of the independent variable f in the ERTBP. Let $[\boldsymbol{X}^{\text{pulse}}, \frac{\text{d}\boldsymbol{X}}{\text{d}f}^{\text{pulse}}]^{\text{T}}$ denote the state generated from Eq. (4) in the pulsating coordinates. Using the normalizing units introduced in the ERTBP, the conversion between $\frac{\text{d}\boldsymbol{X}}{\text{d}f}^{\text{pulse}}$ and $\frac{\text{d}\boldsymbol{X}}{\text{d}t}^{\text{pulse}}$ is given by

$$\frac{\text{d}\boldsymbol{X}}{\text{d}t}^{\text{pulse}} = \frac{1}{r^2} \frac{\text{d}\boldsymbol{X}}{\text{d}f}^{\text{pulse}} \qquad (21)$$

where $r = 1/(1 + e \cos f)$ is the time-varying distance between Mars and Phobos. Equipped with $\frac{\text{d}\boldsymbol{X}}{\text{d}t}^{\text{pulse}}$, the
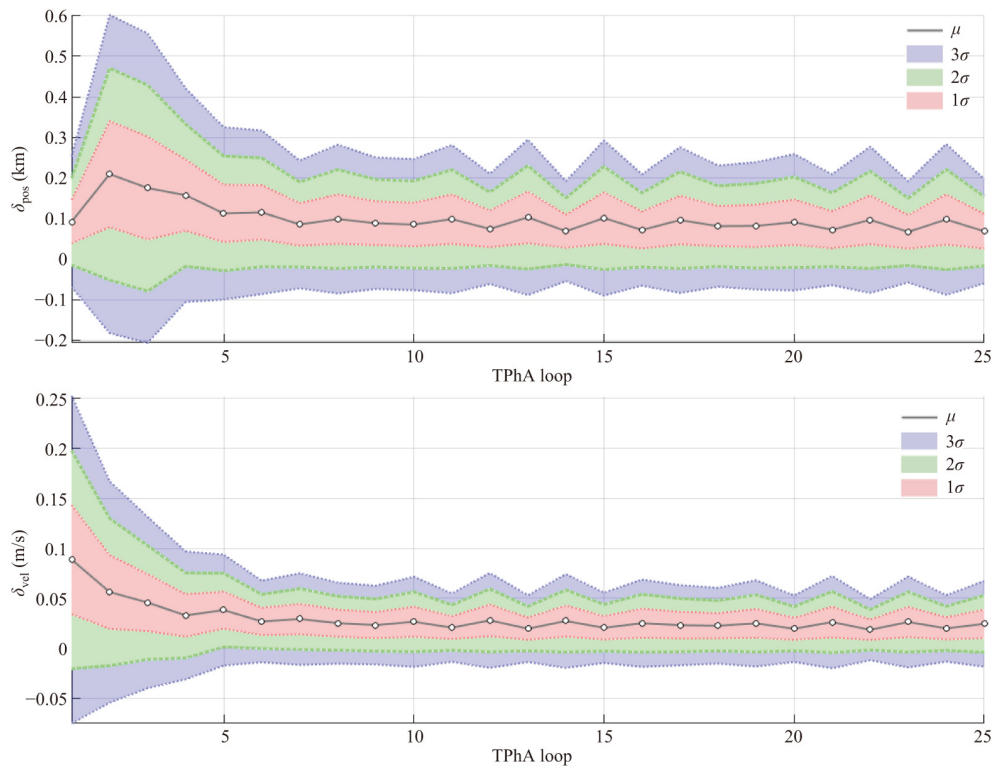
Fig. 5 Position (upper) and velocity (bottom) residuals during station-keeping process based on the CRTBP model with 8 orbital periods per loop.
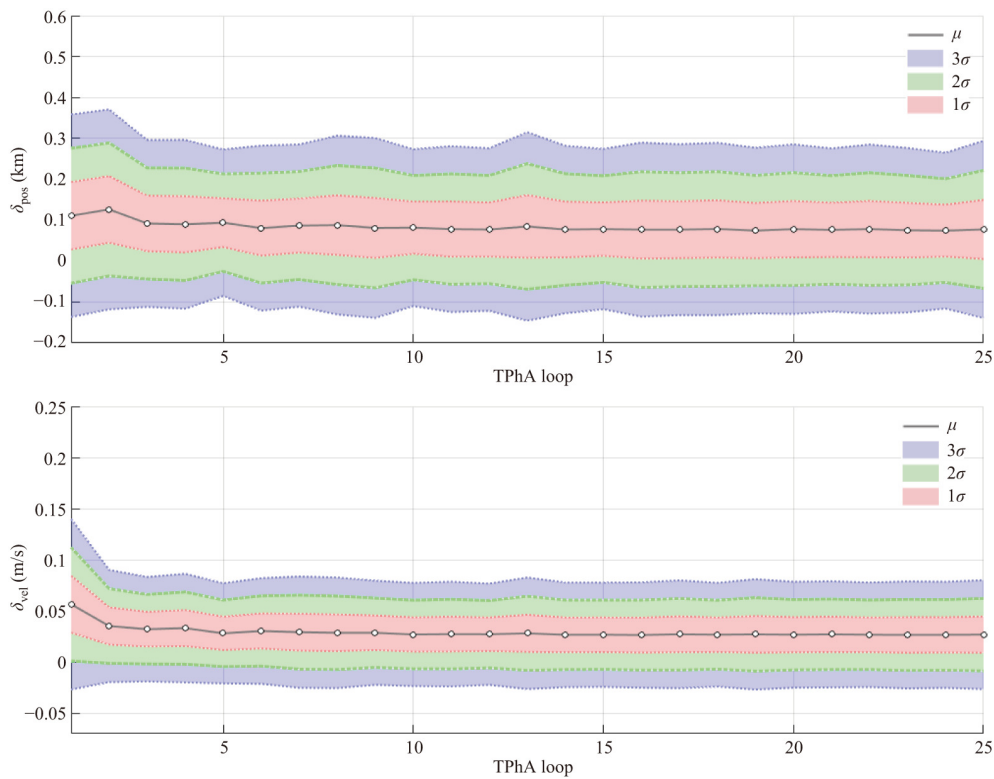
Fig. 6 Position (upper) and velocity (bottom) residuals during station-keeping process based on the CRTBP+EPh model with 8 orbital periods per loop.

transformation from a pulsating state $[\boldsymbol{X}^{\text{pulse}}, \frac{\mathrm{d}\boldsymbol{X}}{\mathrm{d}t}^{\text{pulse}}]^{\text{T}}$ to a non-pulsating state $[\boldsymbol{X}^{\text{nonp}}, \frac{\mathrm{d}\boldsymbol{X}}{\mathrm{d}t}^{\text{nonp}}]^{\text{T}}$ can be derived:

$$
\begin{cases}
\boldsymbol{X}^{\text{nonp}} = r\boldsymbol{X}^{\text{pulse}} \\
\dfrac{\mathrm{d}\boldsymbol{X}}{\mathrm{d}t}^{\text{nonp}} = \dot{r}\boldsymbol{X}^{\text{pulse}} + r\dfrac{\mathrm{d}\boldsymbol{X}}{\mathrm{d}t}^{\text{pulse}}
\end{cases}
\tag{22}
$$

and the resulting non-pulsating state $[\boldsymbol{X}^{\text{nonp}}, \frac{\mathrm{d}\boldsymbol{X}}{\mathrm{d}t}^{\text{nonp}}]^{\text{T}}$ can be used to calculate the input state residual for the maneuver map. An inverse conversion must be conducted once an output maneuver $\Delta\boldsymbol{v}^{\text{pulse}}$ is obtained from Eq. (17). To transform $\Delta\boldsymbol{v}^{\text{pulse}}$ into $\Delta\boldsymbol{v}^{\text{nonp}}$, the provable relationship in Eq. (23) can be utilized:

$$
\Delta\boldsymbol{v}^{\text{pulse}} = \frac{1}{r}\Delta\boldsymbol{v}^{\text{nonp}}
\tag{23}
$$

5.2 Simulation results and analyses

By applying the maneuvers in the manner illustrated in Section 5.1, the feasibility of the TPhA was further investigated in non-autonomous dynamics. As shown in Table 6, maneuver maps generated from the CRTBP+EPh model using the optimal TPhA parameters in Table 5 were adopted in the corresponding station-keeping scenarios for QSO-La in the ERTBP+EPh model. In this case, the periodic QSO-La generated in the CRTBP+EPh was employed to provide reference states for TPhA-based orbital maintenance. Furthermore, all station-keeping configurations remained unchanged for the simulations in the high-fidelity model.

Even though a discrepancy in the dynamic models exists between the map generation and station-keeping simulation, the TPhA maneuvers from the CRTBP+EPh model still adequately fulfill the requirement of station-keeping, with zero failed cases out of 1000 MC samples for all four station-keeping scenarios. It is evident that the

monthly maneuver budget increases when the maneuver maps generated for the low-fidelity model are utilized in the ERTBP+EPh model. The highest monthly maneuver cost of 0.835 m/s was observed when the length of the TPhA loop increased to approximately 48 h. This station-keeping cost is lower than that reported by Baresi *et al.* [17], who reached 6.265 m/s per month.

In addition, the statistics of the station-keeping process corresponding to the last row in Table 6 are presented in Fig. 7. In this case, the position and velocity residuals both reached their plateaus, and the levels were higher than those of their counterparts, as shown in Fig. 6, with the means of the position and velocity residual reaching 0.2 km and 0.15 m/s, respectively. Larger standard deviations were also observed in this case, with the magnitude of 3σ errors increasing to 0.8 km for position and 0.1 m/s. Considering that the simulations for the dynamics ERTBP+EPh were executed using the optimal parameters acquired from simulations based on the CRTBP+EPh models, such an increment in the statistics of residuals is explainable, and the eccentricity of Phobos' orbit exerts a substantial influence on the station-keeping process.

6 Conclusions

In this paper, a novel high-order target phase approach is proposed to overcome the deficiency of the classic target point approach in the station-keeping of periodic orbits in fast dynamics. Two types of crucial polynomial maps, the phase-angle Poincaré map and the high-order maneuver map, were constructed using DA techniques to determine the crucial station-keeping epochs and correction maneuvers. Considering the existence of

Table 6 Staion-keeping results for QSO-La in the ERTBP

Orbital periods per loop	Length of one loop (h)	θ_{EX1} (orbital period)	θ_{EX2} (orbital period)	θ_{TP} (orbital period)	R	S	Dynamic model	Monthly maneuver budget (m/s)	Failed cases
1	5.77	0.748	0.781	1.584	3.73E−3	3.46E−7	CRTBP+EPh	0.491	0
							ERTBP+EPh	0.516	0
2	11.54	0.757	1.443	1.444	1.19E−2	1.78E−7	CRTBP+EPh	0.286	0
							ERTBP+EPh	0.484	0
4	23.08	0.750	0.751	1.443	6.49E−3	1.82E−5	CRTBP+EPh	0.176	0
							ERTBP+EPh	0.242	0
8	46.16	0.877	1.528	2.908	2.36E−1	1.38E−1	CRTBP+EPh	0.362	0
							ERTBP+EPh	0.835	0
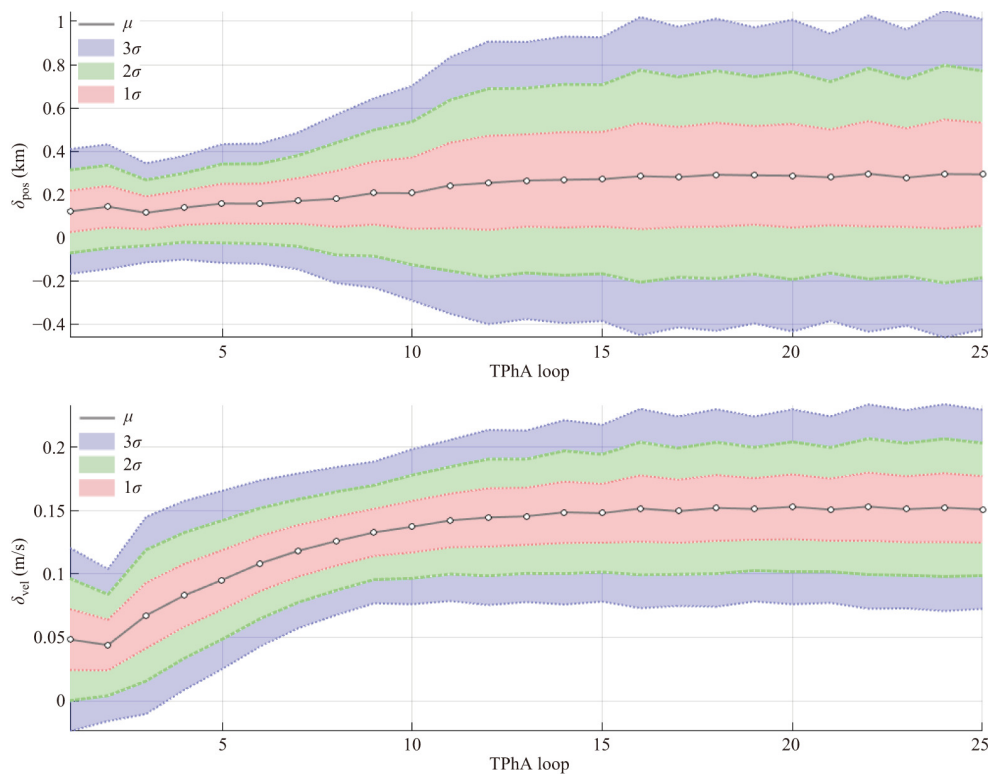
Fig. 7 Position (upper) and velocity (bottom) residuals during station-keeping process based on the ERTBP+EPh model with 8 orbital periods per loop.

uncertainties during orbital maintenance, a TPhA-based stochastic optimization scheme was employed to acquire fuel-optimal and error-robust station-keeping parameters. Station-keeping analyses for QSOs around Phobos validated the efficacy of the proposed TPhA, and a monthly maneuver cost of approximately 1 m/s was achieved in a high-fidelity simulation for a baseline QSO.

Acknowledgements

Declaration of competing interest

The authors have no competing interests to declare that are relevant to the content of this article.

References

[1] Guzzetti, D., Zimovan, E. M., Howell, K. C., Davis, D. C. Stationkeeping analysis for spacecraft in lunar near rectilinear halo orbits. In: Proceedings of the 27th AAS/AIAA Space Flight Mechanics Meeting, San Antonio, TX, USA, **2017**, 160: 3199–3218.

[2] Qi, Y., de Ruiter, A. Station-keeping strategy for real translunar libration point orbits using continuous thrust. *Aerospace Science and Technology*, **2019**, 94: 105376.

[3] LaFarge, N. B., Miller, D., Howell, K. C., Linares, R. Autonomous closed-loop guidance using reinforcement learning in a low-thrust, multi-body dynamical environment. *Acta Astronautica*, **2021**, 186: 1–23.

[4] Zhang, R. K., Wang, Y., Shi, Y., Zhang, C., Zhang, H. Performance analysis of impulsive station-keeping strategies for *cis*-lunar orbits with the ephemeris model. *Acta Astronautica*, **2022**, 198: 152–160.

[5] Folta, D., Pavlak, T., Howell, K., Woodard, M., Woodfork, D. Stationkeeping of Lissajous trajectories in the Earth–Moon system with applications to ARTEMIS. In: Proceedings of the 20th AAS/AIAA Space Flight Mechanics Meeting, San Diego, CA, USA, **2010**: AAS 10-113.

[6] Howell, K. C., Keeter, T. M. Station-keeping strategies for libration point orbit—Target point and Floquet mode approaches. *Spaceflight Mechanics*, **1995**: 1377–1396.

[7] Scheeres, D. J., Hsiao, F. Y., Vinh, N. X. Stabilizing motion relative to an unstable orbit: Applications to

spacecraft formation flight. *Journal of Guidance, Control, and Dynamics*, **2003**, 26(1): 62–73.

[8] Howell, K. C., Pernicka, H. J. Station-keeping method for libration point trajectories. *Journal of Guidance, Control, and Dynamics*, **1993**, 16(1): 151–159.

[9] Gómez, G., Howell, K., Masdemont, J., Simó, C. Station-keeping strategies for translunar libration point orbits. *Advances in Astronautical Sciences*, **1998**, 99(2): 949–967.

[10] Oguri, K., Oshima, K., Campagnola, S., Kakihara, K., Ozaki, N., Baresi, N., Kawakatsu, Y., Funase, R. EQUULEUS trajectory design. *The Journal of the Astronautical Sciences*, **2020**, 67(3): 950–976.

[11] Tos, D. A. D., Yamamoto, T., Ozaki, N., Tanaka, Y., Gonzalez-Franquesa, F., Pushparaj, N., Celik, O., Takashima, T., Nishiyama, K., Kawakatsu, Y. Operations-driven low-thrust trajectory optimization with applications to DESTINY$^+$. In: Proceedings of the AIAA SciTech 2020 Forum, Orlando, FL, USA, **2020**: 2182.

[12] Fu, X. Y., Baresi, N., Armellin, R. Stochastic optimization for stationkeeping of periodic orbits using a high-order target point approach. *Advances in Space Research*, **2022**, 70(1): 96–111.

[13] Ciccarelli, E., Baresi, N. Consider covariance analyses of periodic and quasi-periodic orbits around Phobos. In: Proceedings of the 2021 AAS/AIAA Astrodynamics Specialist Conference, virtual, **2021**: AAS 21-617.

[14] Bernardini, N., Baresi, N., Armellin, R. Orbit maintenance of periodic and quasi-periodic orbits around small planetary moons via convex optimization. In: Proceedings of the 2021 AAS/AIAA Astrodynamics Specialist Conference, virtual, **2021**: AAS 21-626.

[15] Koon, W. S., Lo, M. W., Marsden, J. E., Ross, S. D. Dynamical systems, the three-body problem and space mission design. *Equadiff 99*, **2000**: 1167–1181.

[16] Szebehely, V. *Theory of Orbit: The Restricted Problem of Three Bodies*. New York: Academic Press, **1967**.

[17] Baresi, N., Dei Tos, D. A., Ikeda, H., Kawakatsu, Y. Trajectory design and maintenance of the Martian moons eXploration mission around Phobos. *Journal of Guidance, Control, and Dynamics*, **2020**, 44(5): 996–1007.

[18] Press, W. H., Teukolsky, S. A., Vetterling, W. T., Flannery, B. P. *Numerical Recipes, 3rd edn: The Art of Scientific Computing*. Cambridge, UK: Cambridge University Press, **2007**.

[19] He, Y. C., Armellin, R., Xu, M. Bounded relative orbits in the zonal problem via high-order Poincaré maps. *Journal of Guidance, Control, and Dynamics*, **2019**, 42(1): 91–108.

[20] Berz, M. *Modern Map Methods in Particle Beam Physics*. Cambridge, UK: Academic Press, **1999**.

[21] Fu, X., Baresi, N., Armellin, R. A high-order target point approach to the stationkeeping of near rectilinear halo orbits. In: Proceedings of the 71th International Astronautical Congress, **2020**: IAC-20-C1.6.3, CyberSpace edition.

[22] Tos, D. A. D., Baresi, N. Genetic optimization for the orbit maintenance of libration point orbits with applications to EQUULEUS and LUMIO. In: Proceedings of the AIAA SciTech 2020 Forum, Orlando, FL, USA, **2020**: 0466.

[23] Di Lizia, P., Armellin, R., Bernelli-Zazzera, F., Berz, M. High order optimal control of space trajectories with uncertain boundary conditions. *Acta Astronautica*, **2014**, 93: 217–229.

[24] Wittig, A., Di Lizia, P., Armellin, R., Makino, K., Bernelli-Zazzera, F., Berz, M. Propagation of large uncertainty sets in orbital dynamics by automatic domain splitting. *Celestial Mechanics and Dynamical Astronomy*, **2015**, 122(3): 239–261.

[25] Hénon, M. Numerical exploration of the restricted problem. *Astronomy and Astrophysics*, **1969**, 1: 223–238.

[26] Oberst, J., Wickhusen, K., Willner, K., Gwinner, K., Spiridonova, S., Kahle, R., Coates, A., Herique, A., Plettemeier, D., Díaz-Michelena, M., *et al.* DePhine—the Deimos and Phobos interior explorer. *Advances in Space Research*, **2018**, 62(8): 2220–2238.

[27] Xu, M., Xu, S. J. Exploration of distant retrograde orbits around Moon. *Acta Astronautica*, **2009**, 65(5–6): 853–860.

[28] Campagnola, S., Yam, C. H., Tsuda, Y., Ogawa, N., Kawakatsu, Y. Mission analysis for the Martian Moons Explorer (MMX) mission. *Acta Astronautica*, **2018**, 146: 409–417.

[29] Murchie, S. L., Thomas, P. C., Rivkin, A. S., Chabot, N. L. Phobos and Deimos. In: *Asteroids IV*. Tucson, AZ, USA: University of Arizona Press, **2015**: 451.
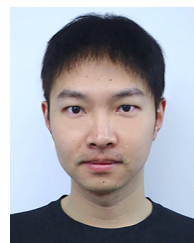
Xiaoyu Fu received his B.Eng. and B.Sc. degrees in aerospace engineering from Beihang University, China, in 2016 and 2019, respectively. He is pursuing a Ph.D. degree at Surrey Space Centre in the University of Surrey, UK. His research interests include trajectory design and spacecraft guidance. E-mail: x.fu@surrey.ac.uk

Nicola Baresi graduated from the University of Colorado Boulder in 2017 with a Ph.D. thesis on spacecraft formation flight and quasi-periodic invariant tori. He later moved to Japan working on the MMX and EQUULEUS missions as a postdoctoral fellow at the Institute of Space and Astronautical Sciences of JAXA. Starting from 2019, Dr. Baresi has joined the University of Surrey, UK, where he is now a lecturer in orbital mechanics at Surrey Space Centre. Nicola is an elected member of the Space Flight Mechanics committee of the American Astronautical Society, as well as a Fellow of the UK Higher Education Academy. E-mail: n.baresi@surrey.ac.uk

Roberto Armellin received his M.Sc. and Ph.D. degrees in aerospace engineering from Politecnico di Milano, Italy, in 2003 and 2007, respectively. Since November 2020, he has been a professor at Te Pūnaha Ātea - Space Institute at the University of Auckland, New Zealand. His current research interests include space trajectory optimization, spacecraft navigation and guidance, and space situational awareness. E-mail: roberto.armellin@auckland.ac.nz